Dynamic Control over Mega-Ampere Electron Currents in Metals Using Ionization-Driven Resistive Magnetic Fields

Y. Sentoku,[2] E. d'Humières,[3] L. Romagnani,[1] P. Audebert,[1] and J. Fuchs[1,*]
[1] *LULI, École Polytechnique, CNRS, CEA, UPMC, route de Saclay, 91128 Palaiseau, France*
[2] *Physics Department, MS-220, University of Nevada, Reno, Nevada 89557, USA*
[3] *Université de Bordeaux, CNRS, CEA, Centre Lasers Intenses et Applications, 33400 Talence, France*

(Received 20 February 2011; published 23 September 2011)

The possibility of dynamically shaping mega-ampere electron currents generated in solids by ultraintense laser pulses in various conductor materials has been investigated. By tuning the target ionization dynamics, which depends both on the target material properties and on the input electron beam characteristics, we can control the growth of resistive magnetic fields that feedback on the current transport. As a result, collimation, hollowing, or filamentation of the electron beam can all be obtained. These results are beneficial for applications such as the production of secondary particles and radiation sources and fast ignition of inertial confinement fusion.

DOI: 10.1103/PhysRevLett.107.135005 PACS numbers: 52.35.Mw, 52.38.Dx, 52.38.Hb, 52.65.Rr

Ultrahigh currents [mega-ampere (MA)] of suprathermal (MeV) electrons, that are driven through solids using relativistic laser pulses (with intensity $I > 10^{18}$ W/cm^2), lie at the heart of numerous applications such as the generation of ultrashort secondary sources of particle and radiation (ions [1], x rays [2], positrons [3], or neutrons [4]), fast ignition of inertial confinement targets [5], or laser-driven hadron therapy [6]. For all these applications, metals are preferred as target materials since they can provide enough cold electron return current to neutralize the forward laser-generated current and allow propagation at current levels (MA) which exceed the Alfvén critical current [7]. At solid density, these beams are not prone to the Weibel electromagnetic two-stream instability [8], since it is collisionally damped [9]. Instead, resistive magnetic fields have been suggested [10–14] to collimate or focus the otherwise divergent electron beams [15,16]. These magnetic fields are driven by the Ohmic fields $E_R = \eta J$ as follows:

$$\frac{\partial \mathbf{B}_R}{\partial t} = -(\eta \nabla \times \mathbf{J} + \nabla \eta \times \mathbf{J}), \qquad (1)$$

where $\mathbf{J}$ is the return current (counterstream of the forward propagating current J_f, $J = -J_f$) and η is the resistivity that dynamically changes during target heating due to the hot-electron flow. Hitherto, hybrid simulations have been used to evaluate the role of such magnetic fields [10–14]. This method, however, presents significant limitations due to its inability to self-consistently model the laser-generated hot-electron source evolving at a dynamically ionizing interface. Therefore, this has limited our understanding of the magnetic field influence and impacted the design [17] of full-scale fast ignition [18].

In this Letter, we demonstrate the importance of the resistive magnetic field and show that we can exploit them to dynamically shape the hot-electron transport in monolithic metals, without having to rely on complex target engineering as, e.g., in Ref. [11]. For this, we couple experimental results with numerical particle-in-cell (PIC) simulations that quantitatively include hot-electron generation, ionization of the target bulk material under ultrafast electron induced heating, and collisions. The idea is that varying the metal target material (i.e., playing with the initial resistivity and heat capacity) and the laser characteristics (i.e., playing with the injected electron beam current density) will allow us to tune the electron transport. This is because varying the resistivity and its gradients in the target [i.e., varying the source term on the right-hand side of Eq. (1)] should induce a variation in the resistive magnetic field pattern and amplitude.

The aforementioned variation in electron transport depending on target material is precisely what we observe in the experimental results shown in Fig. 1. The experiments were performed using the 100 TW short-pulse laser at the Laboratoire pour l'Utilisation des Lasers Intenses (LULI). Laser pulses of ~20–30 J of 1 μm light (350 fs) were focused over 6 μm FWHM at $I_{\max} \sim 6 \times 10^{19}$ W/cm^2 onto the front surface of large (3 mm × 1 cm) various conductor targets with different thicknesses, thus producing Maxwellian electron distribution with mean energies ~1 MeV as recorded using an electron spectrometer (see Fig. 1) [19]. Since the laser absorption is ~40% at these intensities [20] and the average electron energy is ~1 MeV [21], this yields electron currents >MA, which is in line with previous estimates [22]. Since we are interested in studying how the self-generated magnetic fields can modify electrons around the mean energy of the distribution, we used proton imaging of the rear (i.e., of the nonlaser-irradiated) target surface electron sheath as the primary diagnostic, with the protons being detected using a stack of radiochromic films (RCFs) [23] far from the target (see Fig. 1). Indeed, this technique presents two unique

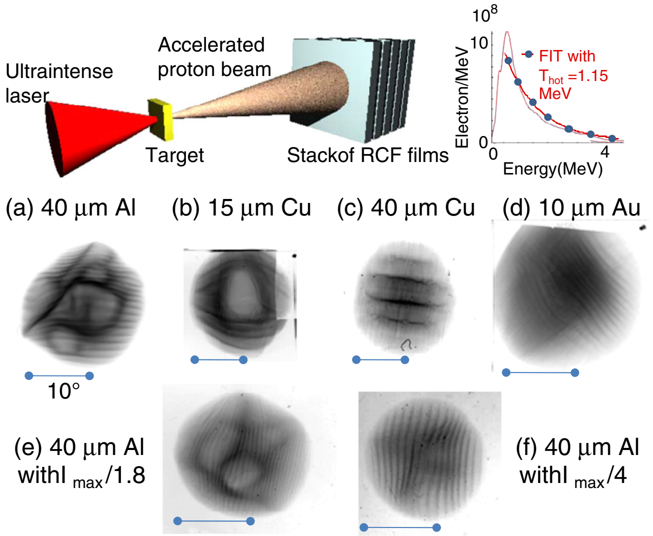

FIG. 1 (color online). (Top, left) Experimental setup. A short-pulse, high energy laser beam irradiates a solid target. Protons originating from the rear target surface are imaged on dosimetric films (RCFs). (Top, right) Electron spectrum recorded by a magnetic spectrometer from a Au 10 μm thick target. (a) Proton image at 6 MeV, 3 cm away from a 40 μm thick aluminum target, (b) same image from 15 μm copper, (c) 40 μm copper, and (d) 10 μm gold targets. For each image, the horizontal bar corresponding to 10° indicates the angular scale of the emitted beam. Cases (a)–(d) are obtained at maximum laser intensity $I_{\max} \sim 6 \times 10^{19}$ W/cm^2. (e) Same image from a 40 μm aluminum target but with a reduced laser intensity (by a factor of 1.8) compared to the images shown in (a)–(d). (f) Same as (e), but here the laser intensity is even more reduced (by a factor of 4).

advantages. First, it allows us to infer the spatial characteristics of the electron sheath, which is the source of the proton acceleration. Second, protons used for the imaging are predominantly accelerated by electrons in the mean energy part of the electron spectrum [24]. This is in contrast with other diagnostics such as, e.g., coherent transition radiation [13] induced mainly by the very high energy electrons which are less likely to be influenced by the self-generated fields studied here. As proton acceleration takes place normally at the local electron sheath surface, it has been shown that any deformation of the electron sheath [25] is reflected in a corresponding modulation of the resulting proton beam angular distribution for all proton energies, i.e., in each RCF layer, the only difference from one layer to the next being a stretching factor of the imprinted modulations [26]. Protons stem from the rear (nonlaser-irradiated) surface of the target [27] by the fast electrons arriving there after having propagated through the foil. There they excite a ~TV/m electrostatic sheath field that ionizes atoms on the surface and accelerates them [23,28,29]. The accelerated ion beam is composed mostly of protons originating primarily from contaminant layers of water vapor and hydrocarbons on the target surface [27]. The spatial distribution of the protons in a given RCF layer gives the angular emission pattern at a specific interval of proton energy with the beam divergence being a function of the energy relative to the maximum energy, as already reported [30].

As for targets, we used Al, Cu, and Au foils. The targets had on their rear surface a periodic grooved pattern. This pattern allowed us to imprint a regular modulation pattern in the angular distributions of the proton beam (as can be seen in Fig. 1) that thus allowed us to image with spatial resolution the accelerating sheath surface [25] and any modulation brought onto it induced by a disturbed transport of the electrons [31].

Figure 1 displays experimental results for various target materials and laser configurations [32]. The recorded images reflect the sheath patterns of the electrons on the rear surface of the target after traversing the solid target. We see strong sheath modulations from a 40 μm thick Al target, see Fig. 1(a), while a 10 μm thick gold target produces a smooth distribution with an intensified peak at the center [1(d)]. The same image from a thin (15 μm) copper target exhibits a doughnutlike distribution (i.e., with a strong proton dose depletion at the center), see Fig. 1(b), while a thicker (40 μm) copper target has a smooth distribution [1(c)]. Note that the thin Cu pattern, though unexplained, was already observed in higher laser intensity experiments [33]. We also observe, as illustrated in Figs. 1(e) and 1(f), that reducing the laser energy, and hence the injected electron beam current, the sheath modulations observed in Al (and also in Cu) progressively decrease to return to smooth distributions, although not as strongly peaked as in the thin Au case.

As shown in Fig. 2, the same behavior is also observed in the simulations. The numerical code we use to analyze the experiments is the two-dimensional PIC code PICLS2D [34], which features binary collisions among charged particles and ionization processes in gas and solid density plasmas. The target is modeled as a uniform slab with a small preplasma with a few micron scale in front of the target. We model targets corresponding to the images shown in Fig. 1, i.e., 40 μm Al, 15 and 40 μm Cu, and 10 μm Au, all with their surface normal oriented along a Cartesian x axis. The target is attached to the transverse boundaries, and we use absorbing boundary condition for particles—i.e., no hot electrons come back inside the target—to represent the large transverse volume of the target. The ion density is set to $50n_c$; here, $n_c = 10^{21}$ cm^{-3} is the critical density for laser wavelength 1 μm. The mass (fully ionized charge) of Al, Cu, and Au ions is $27M_p$ (13), $64M_p$ (29), and $197M_p$ (79), respectively, here M_p is the proton mass. Then the mass density of each target becomes $\rho_{\text{Al}} = 2.2$, $\rho_{\text{Cu}} = 5.3$, and $\rho_{\text{Au}} = 16.9$ g/cm^3. These are close to the mass density of each metal in the laboratory. Initially we set the ion charge state $Z = 3$ for all targets, and the electron density is set to neutralize ion charges.

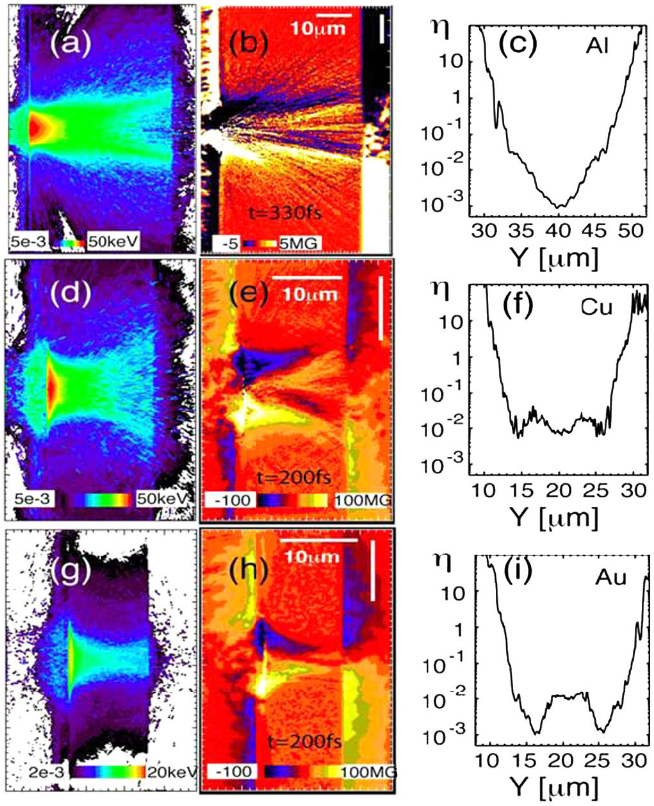

FIG. 2 (color online). PIC simulation results of 40 μm Al (at 330 fs), 15 μm Cu (at 200 fs), and 10 μm Au (at 200 fs) targets. Left column: Electron energy density of (a) Al, (d) Cu, and (g) Au. Center column: Quasistatic magnetic fields of (b) Al, (e) Cu, and (h) Au. Right column: Resistivity profile at 80 fs obtained 1 μm inside the target of (c) Al, (f) Cu, and (i) Au.

Our ionization model is the Thomas-Fermi model in dense plasmas [35]. The electron density increases dynamically during laser irradiation via ionization processes. Initially the particles are at rest, with the initial plasma temperature set to zero. Our spatial (temporal) resolution is 1/50 of the wavelength (τ, laser oscillation period) for Al and Cu targets and 1/100 of the wavelength (τ) for Au target.

Inside the code we calculate the bulk electron temperature by separating hot and bulk electrons with energy of 10 keV, so that the electrons whose energy is less than 10 keV are recognized as bulk electrons. This threshold temperature is selected at the temperature of transition of two temperature distributions in the electron energy spectrum. Note here that the selection of the threshold temperature is insensitive to the calculation of the bulk electron temperature because the temperature is determined by electrons whose energy is less than 1 keV and their population is a few orders of magnitude greater than 10 keV electrons. Using the local bulk temperature and bulk density, we calculate the average ionization degree $Z_{\rm av}$ by the Thomas-Fermi model and ionize atoms to bring the local ionization degree close to $Z_{\rm av}$. In the ionization process, we produce electrons with zero energy and subtract the ionization energy from bulk electrons by shrinking the thermal energy in the cell.

The bulk electron temperature observed in the simulation at 200 fs is ~100 (400) eV inside the Au (Al) target. Since our simulations did not take into account the radiation loss, these temperatures tend to be higher than experimental measurements. Nevertheless, at such temperature (e.g., 100 eV in solid Au) the bound-bound radiation is a minor effect, and the bremsstrahlung radiation is $\sim 10^{15}$ W/cm^2, which is negligible against the electron heat flux.

To clarify the respective roles of the two terms on the right-hand side of Eq. (1), we rewrite it in the simulation coordinates, with x the laser direction, y is transverse, and z is perpendicular to the simulation (x-y) plane:

$$\frac{\partial \boldsymbol{B}_z}{\partial t} = \eta \frac{\partial \boldsymbol{J}_x}{\partial y} + \frac{\partial \eta}{\partial y} \boldsymbol{J}_x. \tag{2}$$

Following the laser Gaussian intensity profile, the current has a peak at the center; namely, the first term naturally becomes positive in the lower side of the simulation box and negative in the upper side. The second term depends on the resistivity gradients that evolve during the laser irradiation through changes in the charge state Z and bulk temperature T as $\eta \propto Z/T^{3/2}$.

For the Al target, the filamentation of the electron current is due to weak resistive magnetic fields that cannot constrain the large injected current. Figure 2(c) shows that η, measured 1 μm inside the target surface at time $t = 80$ fs, i.e., before the resistive magnetic fields start to grow, has its minimum at the center. This is because aluminum has a small heat capacity (hence the temperature peaks at the center) and is ionized to almost full charge state. As a result, the $\partial\eta/\partial y$ term opposes the $\partial J_x/\partial y$ term. This leads to weak fields (dominated by the $\partial J_x/\partial y$ term) of the order of ±5 MG, displayed in Fig. 2(b). The fields form twin channels with many small filaments due to the resistive instability driven by the hot-electron current. As a result, the hot-electron flow, see Fig. 2(a), splits into twin jets (corresponding to a hollow beam in 3D), similar to Ref. [13].

For Au, the situation is significantly different with very strong resistive fields. This is mostly due to the larger heat capacity and the higher ionization level of the high Z Au ions that both concurrently produce a lower bulk temperature at the target center. As a result, as shown in Fig. 2(i), η inside the gold displays a peak at the center. This leads, in Eq. (2), to the resistivity gradient term positively feedbacking on the current gradient term, leading to a more effective growth of the resistive magnetic fields. On top of that, the observed propagation speed of the ionization waves in the Au target is ~4 times slower than that in the Al target, which sustains the growth of the magnetic fields for a longer time. All this leads to fields, shown in Fig. 2(h),

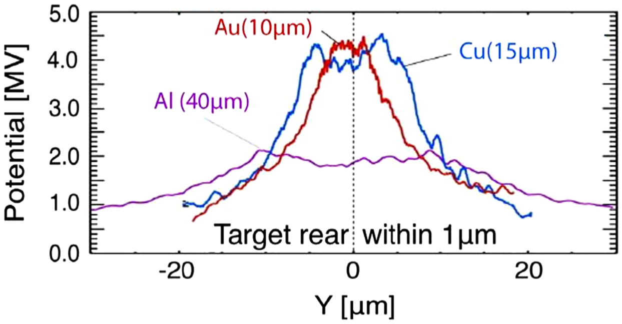

FIG. 3 (color online). Electrostatic potential at the target rear extracted from the PIC simulations and observed at the time when the sheath potential reaches its maximum. These plots are integrated over a distance of 1 μm from the target surface and time averaged over 100 fs.

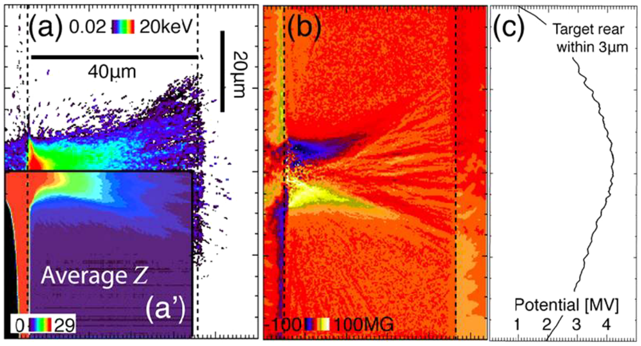

FIG. 4 (color online). PIC simulations results. (a) Upper half: electron energy density, (a') lower half: average Z distribution, and (b) quasistatic magnetic fields at 370 fs for a 40 μm thick Cu target. (c) Electrostatic potential profile at the target rear integrated over 3 μm, and time averaged during 100 fs.

having, contrary to Al, a single channel with amplitude $\sim \pm 100$ MG. Such extreme magnetic fields could represent an interesting platform to study radiation physics under extreme fields. In such magnetic fields, the Larmor radius of the relativistic electron is given by r_L (in μm) $\sim 30 E_{\mathrm{MeV}}/B_{\mathrm{MG}}$, so that the Larmor radius of average energy (~ 2 MeV) electrons becomes less than a micron. The overall outcome is that the hot-electron current is pinched, as seen in Fig. 2(g).

In copper, the resistivity profile, see Fig. 2(f), presents an intermediate case. It displays a twin peak profile due to the competition between heating (T increases) and ionization processes (Z increases) that have opposite effects on η. As a result, the resistive magnetic fields, which have similar amplitude as Au, have twin (hollow) channels, see Fig. 2(e), leading to a hollow beam structure for the hot electrons, as shown in Fig. 2(d). This is similar to Al; however, the mechanism of the formation of the twin beams is different because it is due to spatial modulation of the resistivity.

To compare the simulations to the experiment, we plot in Fig. 3 the electron sheath potential profiles obtained for the different simulations. We integrate the potential over 1 μm from the target surface and time average it over 100 fs from the time when the electrostatic field takes its maximum value. Here, we choose 100 fs as the averaging period because it is the typical time scale of 6 MeV protons as they propagate over a Debye length (~ 1 μm), i.e., the accelerating field length. We see that the 10 μm thick Au target exhibits a single peak distribution with the tightest profile, consistent with Fig. 1(d). The 15 μm thick Cu target, on the other, hand has a twin peak distribution, also consistent with the doughnut pattern of Fig. 1(b). Finally, the 40 μm thick Al target has a lower potential, since it is the thickest target, with a wider and modulated distribution, again consistent with Fig. 1(a). The trends observed in the experiment when increasing the target thickness or reducing the laser energy, i.e., a disappearance of the modulation in Cu or Al, are also observed in the simulations. Figure 4 illustrates a simulation using a 40 μm Cu target. Figure 4(a′) shows that strong ionization ($Z > 15$) proceeds in a distance $x \sim 15$ μm, which is consistent with the heated region seen in the electron energy density map [see Fig. 4(a)]. Thus, strong resistive magnetic fields only grow in this region [see Fig. 4(b)] before breaking into weak ~ 5 MG filaments, which cannot strongly modulate MeV electrons. As a result, the electrons spray out and form a smooth sheath potential at the target rear surface, as seen in Fig. 4(c), consistent with Fig. 1(c). Although not illustrated here, we obtain similar simulation results from reduced laser energy cases.

The technique of manipulating the target resistivity developed here allows, even using a monolithic material, to control MA current flows in solids, e.g., excite the pinching, hollowing, or filamenting of the currents. For this, the target thickness should be equal to or a little thinner than the propagation distance of ionization waves during the laser pulse duration. Beyond the present demonstration, an important practical point is that, keeping the same laser energy but changing the laser intensity (by, e.g., defocusing the laser or increasing the pulse length), one can engineer transporting the same electron charge through a different spatial form, e.g., pinched or hollowed out.

We acknowledge the expert support of the LULI teams and fruitful discussions with P. Antici, S. N. Chen, T. Cowan, and L. Gremillet. The experiments were supported by Grant No. E1127 from Région Ile-de-France and the junior chair program ULIMAC of RTRA-Triangle de la Physique. The work of Y. S. was supported by NNSA/U.S. DOE under Contracts No. DE-PS02-08ER08-16 and No. DE-FC52-06NA27616.

---

*julien.fuchs@polytechnique.fr

[1] V. Malka, Nature Phys. **4**, 447 (2008).
[2] A. Mančić *et al.*, Phys. Rev. Lett. **104**, 035002 (2010).
[3] H. Chen *et al.*, Phys. Rev. Lett. **105**, 015003 (2010).

[4] L. Disdier *et al.*, Phys. Rev. Lett. **82**, 1454 (1999).
[5] M. Key, Nature (London) **412**, 775 (2001).
[6] S. V. Bulanov *et al.*, Phys. Lett. A **299**, 240 (2002).
[7] H. Alfvèn, Phys. Rev. **55**, 425 (1939).
[8] E. S. Weibel, Phys. Rev. Lett. **2**, 83 (1959).
[9] Y. Sentoku *et al.*, Phys. Rev. Lett. **90**, 155001 (2003).
[10] J. R. Davies *et al.*, Phys. Rev. E **56**, 7193 (1997).
[11] S. Kar *et al.*, Phys. Rev. Lett. **102**, 055001 (2009).
[12] A. P. L. Robinson and M. Sherlock, Phys. Plasmas **14**, 083105 (2007).
[13] M. Storm *et al.*, Phys. Rev. Lett. **102**, 235004 (2009).
[14] A. A. Solodov *et al.*, J. Phys. Conf. Ser. **244**, 022063 (2010).
[15] A. Debayle *et al.*, Phys. Rev. E **82**, 036405 (2010).
[16] F. Perez *et al.*, Phys. Plasmas **17**, 113106 (2010).
[17] A. A. Solodov *et al.*, Phys. Plasmas **16**, 056309 (2009).
[18] M. Schirber, Science **310**, 1610 (2005).
[19] M. Allen *et al.*, Phys. Plasmas **10**, 3283 (2003).
[20] Y. Ping *et al.*, Phys. Rev. Lett. **100**, 085004 (2008).
[21] P. Antici *et al.*, Phys. Rev. Lett. **101**, 105004 (2008).
[22] R. Stephens *et al.*, J. Phys. IV **133**, 355 (2006); J. J. Santos *et al.*, J. Phys. Conf. Ser. **244**, 022060 (2010).
[23] R. A. Snavely *et al.*, Phys. Rev. Lett. **85**, 2945 (2000).
[24] P. Mora and T. Grismayer Phys. Rev. Lett. **102**, 145001 (2009).
[25] J. Fuchs *et al.*, Phys. Rev. Lett. **91**, 255002 (2003).
[26] H. Ruhl *et al.*, Phys. Plasmas **11**, L17 (2004).
[27] J. Fuchs *et al.*, Phys. Rev. Lett. **94**, 045004 (2005).
[28] E. Clark *et al.*, Phys. Rev. Lett. **84**, 670 (2000).
[29] S. Hatchett *et al.*, Phys. Plasmas **7**, 2076 (2000).
[30] M. Roth *et al.*, Plasma Phys. Controlled Fusion **47**, B841 (2005).
[31] T. Cowan *et al.*, Phys. Rev. Lett. **92**, 204801 (2004).
[32] P. Antici *et al.*, J. Phys. Conf. Ser. **244**, 022016 (2010).
[33] J. A. Koch *et al.*, Phys. Rev. E **65**, 016410 (2001).
[34] Y. Sentoku and A. J. Kemp, J. Comput. Phys. **227**, 6846 (2008).
[35] Y. T. Lee and R. M. More, Phys. Fluids **27**, 1273 (1984).